# DIII-D Research Towards Establishing the Scientific Basis for Future Fusion Reactors

**C. C. Petty**[1]

The DIII-D Team

[1]*General Atomics, San Diego, CA 92186, USA*
Corresponding Author: C. C. Petty, petty@fusion.gat.com

DIII-D research is addressing critical challenges in preparation for ITER and the next generation of fusion devices through a focus on scientific investigation of plasma physics fundamentals, integration of disparate core and boundary plasma physics, and development of attractive scenarios. Fundamental studies show that including the energetic particle "kick" model in transport codes dramatically improves agreement with the measured beam ion profile during strong Alfvénic activity, while dimensionless parameter scaling studies of intrinsic rotation lead to a predicted ITER rotation profile with significant turbulence stabilization. Hard X-ray spectra measurements show that anomalous dissipation of runaway electron (RE) beams is strongest for low energy RE populations, likely due to interactions between the low energy RE population and RE-driven kinetic instabilities. Core-boundary integration studies show that the small angle slot divertor achieves detachment at lower density and extends plasma cooling across the divertor target plate, which is essential for controlling heat flux and erosion. A rotating $n = 2$ RMP combined with a stationary $n = 3$ RMP has demonstrated access to ELM suppression with lower 3D field strength, while at the same time dynamically controlling the divertor heat and particle flux. Other edge studies show that the higher L-H power threshold with RMP fields is potentially due to both 3D density gradient modifications and changes in $E \times B$ shear layer topology. Super H-mode experiments in the presence of ELMs have achieved near-record pedestal pressures and record stored energies for the present DIII-D configuration with $\beta_{N,ped} \approx 1.3$, $\mathrm{H}_{98}(y,2) \approx 1.6$–$2.4$ and $I_p \leqslant 2.0$ MA. In scenario work, the ITER baseline $Q = 10$ scenario has been advanced by adjusting the early current density profile evolution to obtain reproducibly stable operation with $\approx 0$ external torque and without $n = 1$ tearing modes. In the wide pedestal QH-mode regime that exhibits improved performance, the startup counter torque has been eliminated so that the entire discharge uses $\approx 0$ applied torque and the operating space is more ITER-relevant. Finally, the high-$\beta_\mathrm{p}$ scenario with large-radius ITB has been extended to $I_p \sim 1$ MA ($\mathrm{q}_{95} \sim 6$) with high confinement $\mathrm{H}_{98}(y,2) \sim 1.6$ from both Shafranov shift and negative magnetic shear.

Work supported by the U.S. Department of Energy under DE-FC02-04ER54698.

**Published as a journal article in Nuclear Fusion**
**http://iopscience.iop.org/article/10.1088/1741-4326/ab024a**

# DIII-D RESEARCH TOWARDS ESTABLISHING THE SCIENTIFIC BASIS FOR FUTURE FUSION REACTORS

C.C. Petty for the DIII-D team
General Atomics
San Diego, California, USA
Email: petty@fusion.gat.com

**Abstract**

DIII-D research is addressing critical challenges in preparation for ITER and the next generation of fusion devices through focusing on plasma physics fundamentals that underpin key fusion goals, understanding the interaction of disparate core and boundary plasma physics, and developing integrated scenarios for achieving high performance fusion regimes. Fundamental investigations into fusion energy science find that anomalous dissipation of runaway electrons (RE) that arise following a disruption is likely due to interactions with RE-driven kinetic instabilities, some of which have been directly observed, opening a new avenue for RE energy dissipation using naturally excited waves. Dimensionless parameter scaling of intrinsic rotation and gyrokinetic simulations give a predicted ITER rotation profile with significant turbulence stabilization. Coherence imaging spectroscopy confirms near sonic flow throughout the divertor towards the target, which can account for the convection-dominated parallel heat flux. Core-boundary integration studies show that the small angle slot divertor achieves detachment at lower density and extends plasma cooling across the divertor target plate, which is essential for controlling heat flux and erosion. A rotating $n$=2 RMP combined with a stationary $n$=3 RMP has demonstrated access to ELM suppression with lower 3D field strength, while at the same time dynamically smoothing out the divertor heat and particle flux. The Super H-mode regime has been extended to high plasma current (2.0 MA) and density to achieve very high pedestal pressures (~30 kPa) and stored energy (3.2 MJ) with $H_{98y2}$≈1.6-2.4. In scenario work, the ITER baseline $Q$=10 scenario with zero injected torque is found to have a fusion gain metric $\beta\tau_E$ independent of current between $q_{95}$=2.8–3.7, and a lower limit to the pedestal rotation for RMP ELM suppression has been found. In the wide pedestal QH-mode regime that exhibits improved performance and no ELMs, the startup counter torque has been eliminated so that the entire discharge uses ≈0 injected torque and the operating space is more ITER-relevant. Finally, the high-$\beta_N$ (≤3.8) hybrid scenario has been extended to the high density levels necessary for radiating divertor operation, achieving ~40% divertor heat flux reduction using either argon or neon with $P_{tot}$ up to 15 MW.

## 1. INTRODUCTION

The central theme of the DIII-D research program is to establish the scientific basis and operational knowledge for ITER and future fusion reactors using its unique capabilities. The role of DIII-D in the world's fusion energy program can be understood through three modi: the scientific investigation of plasma physics fundamentals, many of which are portable to other innovative toroidal concepts; understanding how disparate core and boundary plasma physics interact, an issue for all fusion devices in scaling to burning plasma conditions; and the development of attractive scenarios that address critical challenges in preparation for ITER [1] and the next generation of tokamak fusion devices. Scenario development is in many respects the final product of fusion research, where self-consistent, integrated operational regimes for burning plasmas are pursued by a diverse team whose members pool their expertise in different topical science areas. Results contained in the paper have capitalized on several key hardware enhancements in the DIII-D facility, including the small angle slot (SAS) divertor, new power supplies to increase flexibility of applied 3D fields, new types of pellets and tungsten tile inserts, as well as new diagnostics enhancements such as surface-eroding thermocouples, coherence imaging spectroscopy (CIS), an imaging neutral particle analyzer and laser blow off (LBO). Recent results also exploit the existing machine flexibility, e.g., plasma shape control, variable perveance neutral beam injection (NBI), a wide range of NBI torque profiles using a mix of co- and counter-injected beams, adjustable current drive profiles especially from electron cyclotron current drive (ECCD), and variable ion/electron heating profiles.

The paper is organized as follows. Section 2 describes key fusion-enabling advances in disruption mitigation, energetic particle physics, turbulence and transport, and the physics of divertor detachment. Core-Edge integration is discussed in Section 3, encompassing the newly-installed SAS divertor that gives detachment at lower core collisionality, the effect of divertor closure on pedestal structure, the impacts of resonant magnetic perturbations (RMP) on the plasma edge and L-H transition, and high pedestal pressures in Super H-mode. Advances in low-torque operation of both the ITER baseline scenario (including with RMP ELM-suppression) and the quiescent high confinement mode (QH-mode), the extension of the high-$\beta_P$ regime to lower safety factor using reverse magnetic shear, and the integration of the high-$\beta_N$ hybrid scenario with a radiative divertor are described in Sec. 4. Finally, Section 5 gives a summary of achievements and discusses planned upgrades and the future direction of the DIII-D program.

## 2. ADVANCES IN FUSION ENERGY SCIENCE

Foundational science studies encourage in depth study of physical mechanisms that underpin key fusion goals. In this section, advances in fusion energy science from recent DIII-D experiments will be discussed in the disruption, energetic particle, turbulent transport and boundary physics areas.

As full current disruptions in ITER may damage the first wall and vessel components if left unmitigated, DIII-D research places a high priority on establishing the principles and techniques for ITER's disruption mitigation system. Experiments on DIII-D have injected multiple shattered pellets at different toroidal locations for the first time [2], as is planned for the ITER disruption mitigation system. Systematically varying the relative timing of the two shattered pellets suggests that simultaneously injected pellets may impact the assimilation of each other, altering the resulting disruption characteristics compared to that due to a single pellet injecting similar neon quantities. As seen in Fig. 1(a), thermal quench (TQ) radiation fractions measured near the injection location are reduced with the dual pellets, possibly as a result of a more rapid shutdown due to a broader impurity distribution over multiple flux tubes. Figure 1(b) shows that mitigation of current quench loads is also similarly reduced in the dual pellet cases, consistent with the observed reduction in TQ mitigation. These results suggest that extrapolating single pellet results to ITER may underestimate the required injection quantities for its multiple-pellet disruption mitigation system.

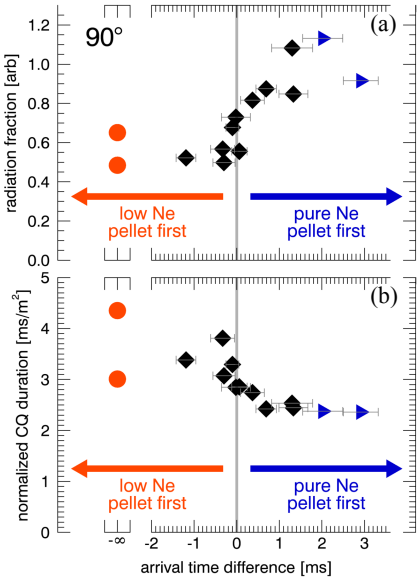


*FIG. 1. Dependence of disruption mitigation metrics on relative timing of pellets.*

New energy-resolved measurements of hard X-ray (HXR) flux identify dissipation mechanisms for runaway electron (RE) populations that may arise after a disruption. Measurements with a unique gamma-ray imaging (GRI) system demonstrate that the observed anomalous dissipation (cast in terms of the applied electric field $E$ significantly exceeding the critical electric field $E_{crit}$) of RE beams is strongest for low energy RE populations [3,4]. This can be largely understood by including the self-consistent interaction of the RE population with RE-driven kinetic instabilities that arise from strong wave-particle interactions with the low energy RE population (Fig. 2(a)) [5]. These kinetic instabilities ($\omega >> \omega_{ci}$, existing above 100 MHz) are directly observed using high-frequency magnetic pick-up loops in quiescent RE regime [6-8]. Additionally, a lower frequency mode ($\omega << \omega_{ci}$) triggered by RE following massive argon injection is found to suppress RE beam formation. Spatiotemporally resolved HXR measurements using the GRI system have also validated RE distribution function *f(E)* dependencies, demonstrating that decreasing synchrotron damping shifts the high-energy *f(E)* towards higher energy, and increasing collisional damping shifts the full *f(E)* to lower energy. Agreement between the predicted and measured *f(E)* is greatly improved when the effect of kinetic instabilities is included (Fig 2(b)). Observation of these instabilities and their effect on RE dissipation both improves confidence that model-based optimization of RE avoidance and mitigation can be achieved and opens possible new avenues for RE control.

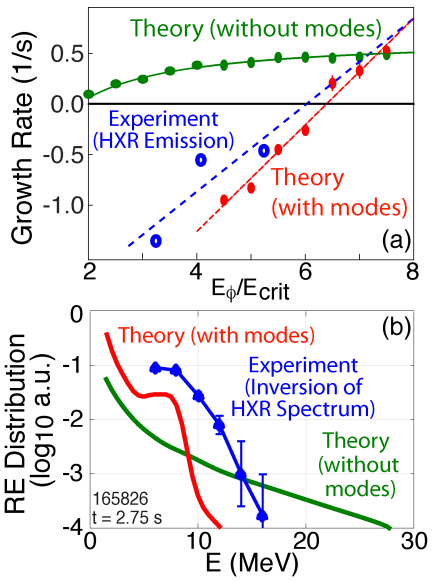


*FIG 2. Comparison of theoretical (with and without kinetic instabilities) and measured (a) RE growth rates and (b) f(E).*

The inclusion of a reduced physics model for EP transport, known as the *kick model* [9], in TRANSP has resulted in a dramatic improvement in simulating the fast-ion transport during strong Alfvénic activity and tearing modes [10]. Fast-ion transport driven by MHD instabilities can be detrimental to plasma performance on DIII-D and in future burning plasma devices. Figure 3 examines a discharge containing a large 2/1 neoclassical tearing mode (NTM), where the deviation between the measured and (classically) simulated neutron rates indicate substantial fast ion transport. Converting the measured NTM island width into the input mode amplitude for the kick modeling gives a resulting neutron rate that compares well to experiment. Alternatively,

if the amplitude of the NTM used in the kick modeling is adjusted to match the measured neutron rate, then good agreement is obtained between predicted and measured NTM island amplitude (Fig. 3(a) inset) and FIDA signal for counter-passing ions (Fig. 3(c)), as well as satisfactory FIDA agreement for co-passing ions (Fig. 3(b)).

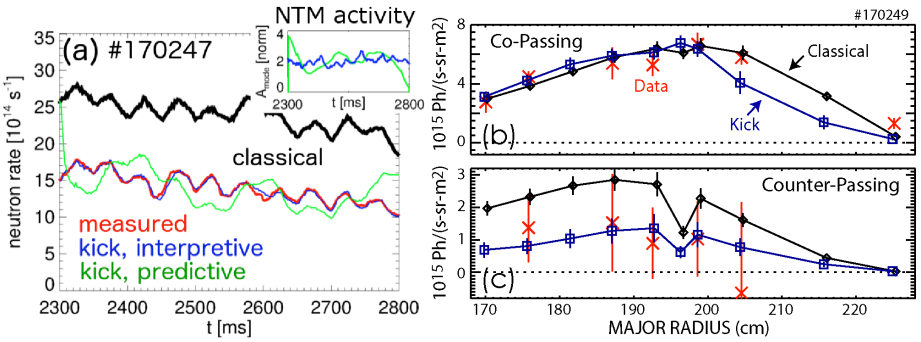


*FIG 3. (a) Neutron rate from TRANSP modeling compared to measured rate. The inset shows the mode amplitude from interpretive kick model analysis (blue) and experiment (green). Radial profiles for FIDA signals for (b) co- and (c) counter-passing fast ions from TRANSP (green and blue lines and symbols) and experiment (red symbols).*

The phase space resolution implemented in the kick modeling is crucial for reproducing details of the measured beam ion profile from FIDA. Enhancements to TRANSP via the inclusion of reduced EP transport models enable scenario development and predictions including realistic treatment of fast ion transport by instabilities.

The predicted toroidal rotation profile in ITER from intrinsic and NBI sources is significant enough to have a stabilizing influence on turbulent transport, thereby enhancing ITER's fusion performance. The measured ρ* and ν* scaling of intrinsic torque with NBI sources predicts an edge rotation in ITER of 10 krad/s [11], while a dimensionless empirical scaling for intrinsic rotation gives a slightly lower value of 4 krad/s [12]. Using the lower value, Fig. 4 shows that the predicted rotation profile for the ITER baseline scenario (IBS) made with the TGYRO and TGLF transport model, and including the NBI torque, has enough ***E×B*** shear to double the D-T fusion gain compared to no shear simulations [13]. While these initial experiments were conducted using NBI heating, subsequent experiments in ECH H-mode plasmas find a similar ρ* scaling of intrinsic angular momentum, showing that fast ions did not influence the previous results. Additionally, differences in intrinsic rotation for closed and open divertor configurations are small, showing that momentum transport due to neutrals in the pedestal is not a significant hidden variable. Besides the effect on turbulence, the toroidal rotation profile in ITER may affect ELM suppression physics, as discussed in Sec. 4.

An investigation of metallic impurity transport using the recently installed LBO system in DIII-D [14] demonstrates little core accumulation of aluminum in ITER-relevant H-mode plasmas. Measuring metallic impurity accumulation is beneficial for constraining multi-channel transport models and helps to predict fuel dilution in ITER. By varying the mix of electron cyclotron heating (ECH) and NBI, the transport of a trace amount of aluminum has been probed for H-mode plasmas with $T_e/T_i$=0.7 and 1.6 at fixed density ($4\times10^{19}$ m$^{-3}$) and fixed beam torque (2 Nm). Propagation of the aluminum is monitored by a combination of fast soft-X ray

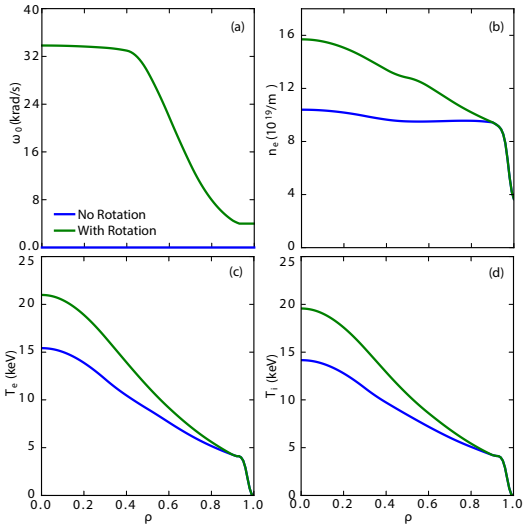


*FIG 4. Predictions of ITER baseline scenario from TGYRO and TGLF, with and without **E×B** shear effects: (a) toroidal rotation, (b) electron density, (c) electron temperature and (d) ion temperature.*

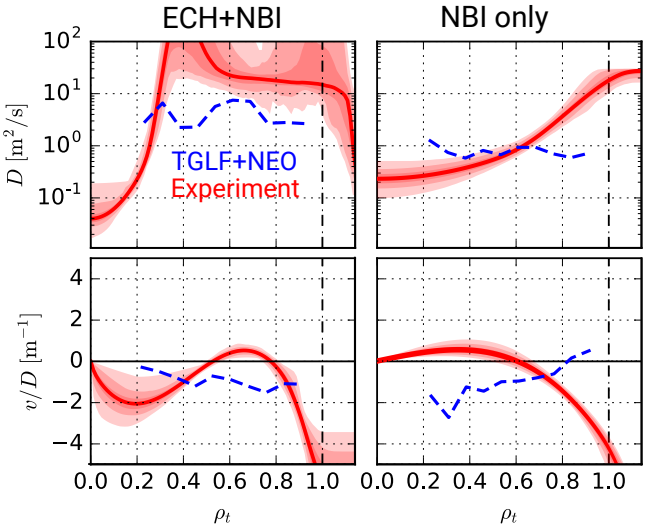


*FIG. 5. Measured aluminum diffusion and density peaking factor (red lines) for ECH+NBI with $T_e/T_i$=1.6 and NBI only with $T_e/T_i$=0.7. Modeled aluminum transport from TGLF and NEO are also indicated (dash blue lines).*

diagnostic and charge exchange spectroscopy of the fully striped ions. Using the STRAHL model, the transport coefficients that best reproduce the observed emissivity evolution are shown in Fig. 5 by red confidence bands. A large increase in impurity diffusion at $T_e/T_i$=1.6 is observed just outside of the ECH location at ρ=0.25, while the density peaking factor *v/D* is small in both cases. Aluminum transport predictions from the TGLF-SAT0 transport model [15] and NEO neoclassical code [16], indicated by blue dashed lines in Fig. 5, similarly find a small value of *v/D*. While the modeled aluminum diffusion for the $T_e/T_i$=1.6 case is 5–10 times larger than the $T_e/T_i$=0.7 case, it is below the experiment value during ECH. Future experiments using the LBO system on DIII-D will extend these impurity transport studies in ITER-relevant conditions to higher-Z ions like tungsten.

Studies of negative triangularity ($\delta$) shape find reduced fluctuations and H-mode like confinement ($H_{98y2}$=1.2) in plasmas with L-mode like edge pressure profiles and no ELMs. These experiments used a combination of ECH and NBI to explore regimes with $T_e/T_i$>1 and $T_e/T_i$~1 [17]. Preliminary fluctuation data shows negative $\delta$ plasmas have lower levels of density and electron temperature fluctuations, typically reduced by 20% in the region 0.7<ρ<1.0, compared to equivalent positive $\delta$ discharges. A linear gyrokinetic analysis indicates that improved core confinement in negative δ discharges is from reduced growth rates in the spectral region $k_\theta\rho_s$<2 due to effect of shape on the dominant TEM modes, as well as from increased Shafranov shift and higher plasma rotation. High beta ($\beta_N$=2.6) operation has also been achieved in negative $\delta$ plasmas with L-mode edge.

In boundary physics, a primary method of reducing the divertor heat flux is to establish highly radiating boundary plasmas with cold, dissipative conditions in front of the divertor targets ("detachment"). As shown in Fig. 6, UEDGE multi-fluid simulations with cross-field drifts (***B*×∇*B***-drift towards the X-point) have been able to reproduce the experimentally observed step-like onset of divertor detachment (difference between the black and red symbols and lines) in H-mode plasmas by running simulations with different neutral density conditions in the divertor but the same upstream separatrix density and boundary conditions [18,19]. The bifurcation of the divertor solution between the attached and detached branches is being driven by the non-linear dependence of divertor ***E*×*B***-drifts on the divertor conditions and potentials. In low density, high temperature attached conditions, the strong radial potential gradient between the common scrape-off layer (SOL) and private flux region (PFR) drives a poloidal ***E*×*B***-drift from the low field side (LFS) to the high field side (HFS) divertor, maintaining low density, high temperature attached conditions. As the divertor evolves towards detachment, the strong radial potential gradient between common SOL and PFR is reduced, diminishing the ***E*×*B***-drift particle sink in the LFS divertor leg. As a result, the LFS divertor leg can evolve non-linearly to strongly detached conditions with minimal change in the upstream SOL plasma density.

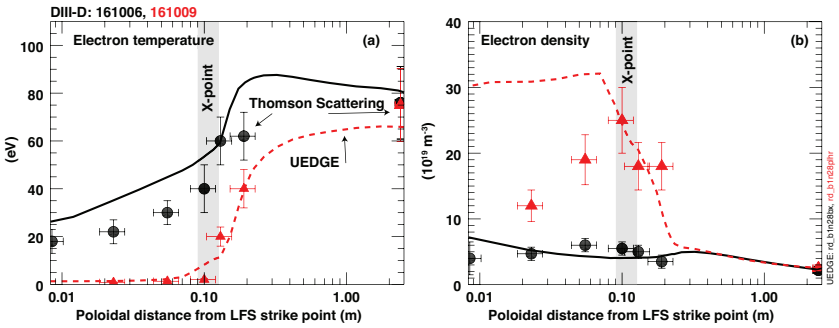


*FIG. 6. Measured and simulated (a) electron temperature and (b) electron density along a flux tube in the LFS SOL. Black symbols and line are an attached case, red is a detached case. The UEDGE simulations correspond to $\Psi_N$=1.0009.*

The excellent divertor diagnostics on DIII-D have been used to characterize the upstream SOL conditions and divertor parallel transport in detached H-mode plasmas [20]. Experiments find that the midplane separatrix density increases approximately as the square root of the parallel heat flux, as expected from analytic 1-D models of conduction dominated heat flux. However, the divertor density does not increase with power as expected, indicating that parallel convection (rather than conduction) carries a significant fraction of the power through the radiating zone, expanding the radiating region from the X-point towards the divertor target. Imaging of the C-III flow

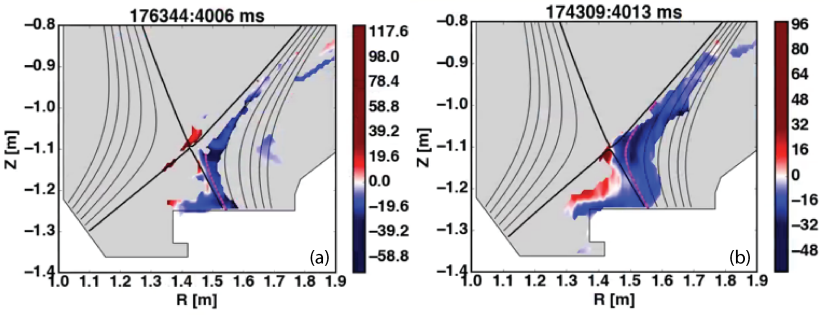


*FIG. 7. CIS image of toroidal flow of C-III impurity for (a) 3 MW case and (b) 13 MW case. Negative flow velocity (blue) is towards the divertor target.*

velocity by CIS, shown in Fig. 7, finds a parallel plasma flow towards the divertor target at near the sound speed ($M$~1), which can account for the observed parallel heat flux profile (not shown). In addition, a significantly larger volume of C-III emission in the divertor with higher power indicates increased radial transport, leading to a broader density profile.

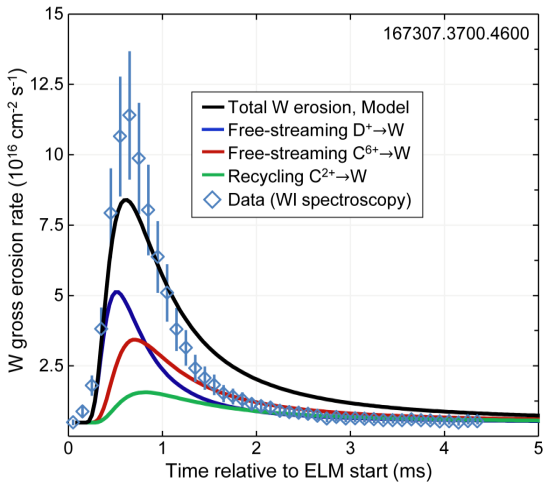


*FIG. 8. FSRM predictions of the gross erosion rate of tungsten vs. ELM time with the contributions from different W erosion pathways identified. Measurements inferred from W-I spectroscopy are overlaid.*

As ITER will have stringent limits on tungsten (W) core contamination, recent model validation studies have sought to improve the understanding of high-Z gross and net erosion in a mixed-materials divertor environment through benchmarking against DIII-D PMI experiments. ERO modeling of L-mode DiMES experiments and results from the DIII-D experiments with W rings embedded in the lower divertor indicate that high-Z erosion and migration in the DIII-D divertor is strongly influenced by the transport and deposition of low-Z impurities. Particle-in-cell modeling with the SPICE code indicates that small perturbations of the plasma sheath can lead to a strong reduction of the local divertor recycling flux, which is observed in experiments [21]. In addition, a refined model for the ELM heat and particle flux to the divertor, the free-streaming plus recycling model (FSRM), has been validated against DIII-D databases of ELM ion fluence and W gross erosion measurements. The FSRM is found to be consistent with DIII-D data across a wide range of pedestal and divertor conditions using a constant value of 0.96 for the effective particle recycling coefficient [22]. The conclusion is that energetic free-streaming $D^+$ ions and $C^{6+}$ impurities from the pedestal top typically dominate the intra-ELM gross erosion of W in the DIII-D divertor (Fig. 8). This understanding supports the idea of replacing carbon with lower Z ions (Li, Be) for better erosion control, plasma impurity content, and tritium retention in future fusion reactors

## 3. CORE-EDGE INTEGRATION

Developing fully integrated core-pedestal-SOL-divertor solutions remains a significant challenge for magnetic fusion, spanning plasma physics, atomic physics, and plasma-material interactions. Understanding these linkages to inform solutions is the goal of core-edge integration research.

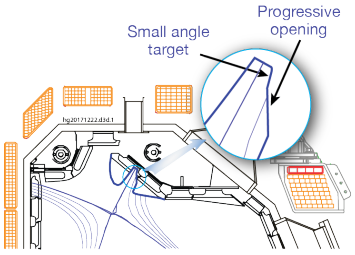


*FIG. 9. Prototype SAS divertor.*

A Small Angle Slot (SAS) divertor has been installed on DIII-D (Fig. 9) to further evaluate the role of divertor closure in achieving efficient heat dispersal required for steady-state tokamaks. SAS was designed to both enhance neutral trapping and optimize neutral distribution along the target to achieve strong plasma cooling across the divertor at a lower upstream plasma density [23]. Experiments have found a strong impact of drifts on SAS operation, and showed that with the ion $\boldsymbol{B}\times\nabla\boldsymbol{B}$-drift away from the X-point SAS can achieve, relative to both the open LSN divertor and the more closed USN divertor, (i) a significant reduction of the electron temperature across the divertor target and (ii) access to dissipative divertor operation with $T_e$ < 10 eV over a wider range of H-mode operational densities. As seen in Fig. 10, SAS divertor obtains detachment at lower density for well-matched discharges without impurity radiation enhancement at $I_P$~1 MA and $P_{NB}$~4 MW [24].

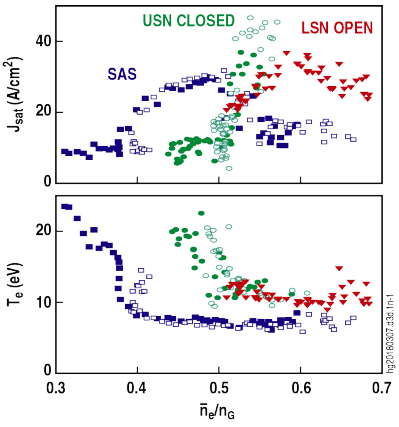


*FIG. 10. Comparison of Langmuir probe ion saturation current density (top) and electron temperature (bottom) near strike point vs. density for SAS (blue), open lower divertor (red) and more closed upper divertor (green).*

The SAS discharges exhibit less degradation in H-mode confinement factor with increasing edge pedestal density than the open LSN divertor or more closed USN divertor for similar conditions, as plotted in Fig. 11. Detailed transport and pedestal stability analyses find that the better confinement with SAS is associated with improved pedestal temperature and pressure, which are primarily due to an increased

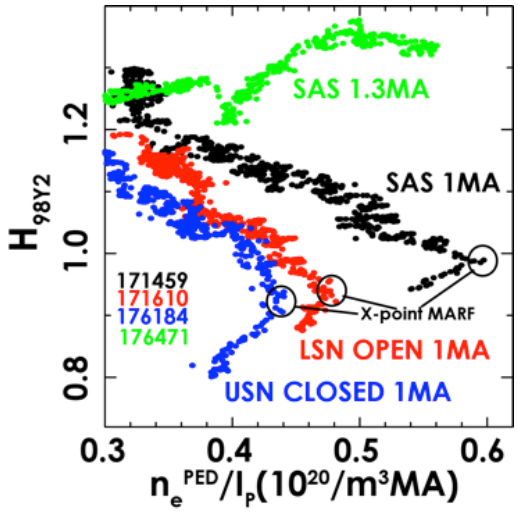


*FIG. 11. Comparison of confinement factor vs. pedestal density normalized to plasma current for different divertor configurations. Densities for X-point MARFE formation are also indicated.*

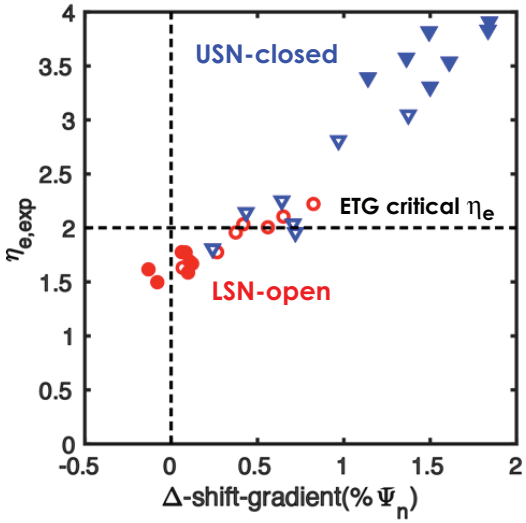


*FIG. 12. Variation of $\eta_e$ at maximum pedestal electron pressure gradient in open and closed divertor geometries vs the difference between locations of maxima of $n_e$ and $T_e$ gradients. Filled symbols are for partially detached divertors.*

pedestal width. Also shown in Fig. 11 are the densities where an X-point MARFE results in further confinement reduction (circled points). For the SAS discharges, there is a greater range of density between detachment onset and X-point MARFE formation, thus widening the window for detachment control and facilitating core-edge integration.

Experiments studying neutral particle fueling indicate that a lower particle source inside the separatrix from higher SOL opacity is not necessarily a barrier to raising the pedestal density [25]. Relating the midplane filterscope signals to the neutral density gives evidence that the ionization front is pushed further out into the SOL during strong gas puffing, increasing the opaqueness to neutrals. An up-down asymmetry in the electron density on closed surfaces (i.e., higher densities closer to X-point) is measured for the first time in ELMing H-mode on DIII-D at higher fueling rates. While the measured change in the edge density during gas puff modulation shows that direct neutral fueling is inefficient for opaque SOL conditions, the outer divertor leg appears to detach with increasing opacity/SOL density, which can explain the continued increase in pedestal density if the ionized plasma in the SOL flows to the divertor and there recycles, proving a new opportunity to fuel the core plasma.

Experiments find that divertor geometry, and specifically divertor closure (the ability to confine neutrals), can be used as a tool to change the pedestal structure to allow the probing of pedestal transport over a range of $n_e$ and $T_e$ gradients [26]. On DIII-D, an open divertor configuration can be obtained with discharges in a LSN configuration with the outer strike point (OSP) on the lower shelf, while a closed configuration can be obtained with a USN configuration with the OSP in the throat of the baffled upper pump. Modeling with both OEDGE and SOLPS shows that for similar $T_e$ and $n_e$ profiles at the OSP, the closed divertor has a significant reduction (30–40%) in the amount of core ionization as compared to the open divertor. For a fixed pedestal density, the closed divertor has a higher separatrix density and allows access to pedestals with a larger outward shift of the electron density gradient relative to the electron temperature gradient than are obtained with the open divertor. The ratio of $\eta_e = L_{ne}/L_{Te}$, with $L_{ne}$ and $L_{Te}$ being the $n_e$ and $T_e$ scale lengths respectively, increases approximately linear with the gradient shift parameter such that $\eta_e$ is varied by more than a factor of two, as seen in Fig. 12. The high values of $\eta_e$ achieved (~4) show that a large gradient of $T_e$ can be maintained even with flattening of the density pedestal. This is a promising result for ITER, which is predicted to have a flat density pedestal.

Impurity experiments using $n$=3 RMP fields to suppress ELMs in ITER-shaped plasmas found a factor of 2–3 reduction in the effective helium particle confinement time compared to ELMing H-modes without RMP fields [27]. Measurements of neutral partial pressures in the pumping plenum from Penning gauges show the partial pressure of helium increases substantially more than that of deuterium during RMP ELM-suppression for a range of cases, in comparison with ELMing cases. This result suggests that RMP fields can generate adequate helium ash removal in ITER in the absence of ELM events.

DIII-D has made major advances in using 3D magnetic fields to extend ELM suppression and pedestal performance. Reduced ELM suppression thresholds and dynamic divertor control have been obtained using a rotating $n$=2 RMP combined with a stationary $n$=3 RMP [28]. Experiments have demonstrated that using mixed toroidal harmonic RMP for ELM suppression lowers the threshold coil current by ~10% (a 30% decrease in the equivalent current of total energy) compared to a RMP with a single toroidal harmonic number. In these experiments, $n$=2 RMP is only able to mitigate ELMs, while complete ELM suppression is achieved with $n$=3

RMP. For the ELM mitigation case, a linear dependence of the plasma response on the applied field is measured, but when the two RMPs are combined a jump up in $n$=3 plasma response is observed during the transition from ELM mitigation to suppression. This jump is a non-linear bifurcation that indicates the $n$=2 field helps to penetrate the $n$=3 mode which leads to ELM suppression. MHD simulation with the MARS-F code shows good agreement in both mode structure and phase from magnetic sensors during ELM mitigation, although during ELM suppression the modeling has an unexplained phase shift relative to the observed plasma response in DIII-D. Prominent heat flux splitting in the divertor is observed in these experiments for n=3 RMP, as seen in Fig. 13, while variation of the heat flux splitting pattern is observed when n=2 RMP is added at different phases. The particle flux footprint on the divertor shows a similar behavior as the heat flux. These patterns are qualitatively consistent with modeling of field penetration depth using TOP2D with plasma response modeled by MARS-F. Therefore, the fine structure in the divertor heat and particle flux during ELM suppression can be smoothed out during a full cycle of a rotating $n$=2 RMP (combined with a static $n$=3 RMP). These results expand the physics understanding and potential effectiveness of this multi-harmonic technique for reliably controlling ELMs and divertor power/particle loading distributions in future burning plasma devices as ITER.

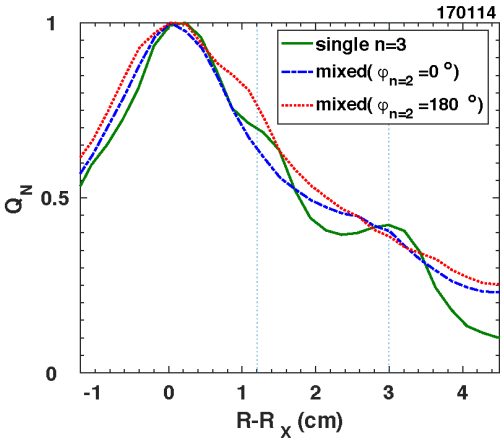


*FIG. 13. Measured divertor heat flux profiles for pure n=3 RMP (green), and additional n=2 RMP with phase 0° (blue) and 180° (red). Vertical lines mark additional peaks locations.*

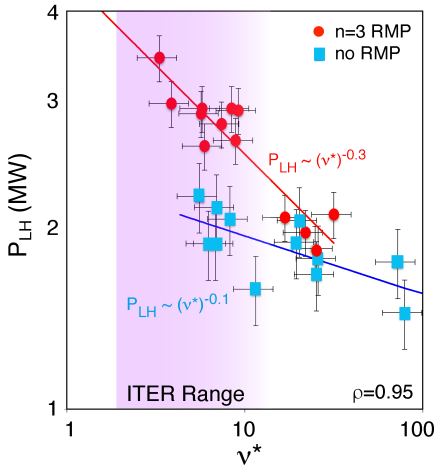


*FIG. 14. L-H transition power threshold vs. collisionality with and without applied n=3 RMP ($3.3\times10^{-4} \le \delta B/B \le 4.6\times10^{-4}$). The expected ITER L-mode edge collisionality range is shaded.*

Studies on DIII-D find that the increase in H-mode threshold power from $n$=3 RMP becomes larger for ITER-relevant collisionalities, which is potentially a concern for ITER since RMP may have to be applied prior to the L-H transition to safely suppress the first ELM. Experiments in the ITER similar shape (ISS) with a mix of ECH and balanced NBI, $\langle n_e \rangle$=1.5–5×$10^{19}$ $m^{-3}$ and $q_{95}$~3.6 demonstrate that the L-H power threshold with applied RMP increases with decreasing collisionality like $P_{LH} \sim \nu_*^{-0.3}$, compared to non-RMP plasmas where $P_{LH} \sim \nu_*^{-0.1}$, as seen in Fig. 14 [29]. The L-H power threshold is impacted above a threshold $\delta B/B \sim 2.5\times10^{-4}$, which is below the ELM suppression threshold. Similar to earlier RMP investigations in L-mode plasmas [30], a reduction in radial electric field ($E_r$) well and ***E×B*** shear, along with an increase in long wavelength turbulence measured by beam emission spectroscopy (BES), is observed just before the L-H transition. Edge magnetic stochasticity provides an attractive explanation of the edge plasma modifications and increase in $P_{LH}$ with RMP, and the more pronounced decrease in edge $E_r$ well at low $\nu_*$ is consistent with a simple fluid model describing stochastic electron current flow. Preliminary experiments indicating that $n$=3 non-resonant magnetic perturbations give rise to smaller changes in $E_r$ and ***E×B*** shear suggest there is room for optimization of the RMP spectrum with less effect on $P_{LH}$.

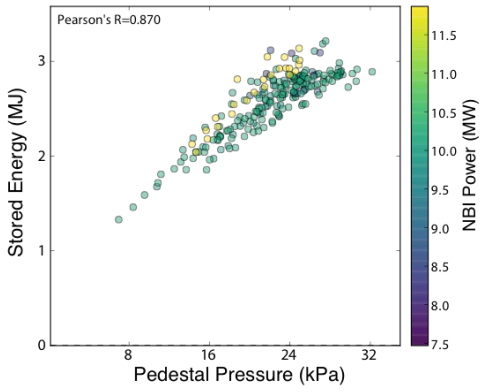


*FIG. 15. Plasma stored energy from EFIT vs. pedestal pressure from Thomson scattering (×2) for Super H-mode experiments.*

Finally, the Super H-mode regime, which achieves high confinement and high beta through an elevated pedestal height and broad profiles [31,32], has been utilized to create high fusion performance plasmas with reduced divertor heat flux. Super H-mode is predicted by the EPED model to occur in strongly shaped plasmas where the pedestal solution remains peeling limited (pressure increasing with density) up to very high density. By extending the Super H-mode regime to high $I_P$ (up to 2 MA), very high pedestal pressures (~30 kPa) and record stored energies (3.2 MJ) for the present DIII-D vessel

configuration have been transiently achieved [33], as shown in Fig. 15, with $\beta_{N,ped}$=1.3 and $H_{98y2}$=1.6-2.4. During the density rise phase shortly after the L-H transition, the Super H-mode attains peak values of D-T equivalent fusion gain that are the highest achieved (=0.45) on any medium scale (R<2 m) tokamak. By applying a small $n$=3 RMP to the Super H-mode regime to control the density and impurity accumulation, good performance has been sustained for ~3 s at $\beta_N$=2.9, $H_{98y2}$=1.6 and nearly 2 MJ of stored energy. Because the pedestal in Super H-mode is limited by current-driven modes, it is predicted that the near separatrix density can be increased to enable attractive divertor solutions while remaining compatible with high fusion performance in the core. New experiments have employed $D_2$ and $N_2$ gas puffing to improve divertor conditions. High pedestal pressure (>20 kPa) and core confinement are sustained in a strongly radiating divertor with a high gas puff rate and more than a factor-of-2 reduction in divertor electron temperature.

## 4. SCENARIO DEVELOPMENT

Research into scenario development aims to unite all of the elements needed for a specific burning plasma mission. In this area, recent DIII-D activity has emphasized the coupling of stable, low-rotation inductive scenarios to various methods of ELM suppression, as well as joining a high power, high beta core to a radiative divertor solution.

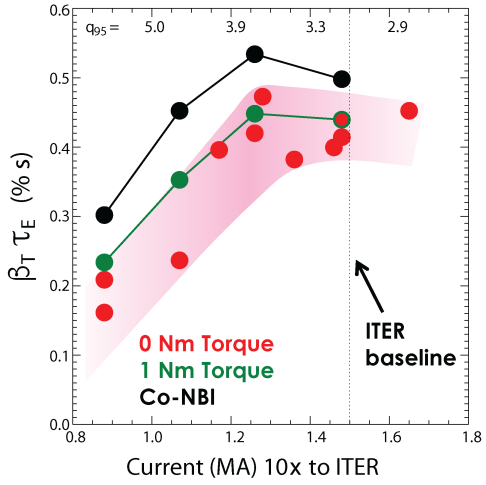


*FIG. 16. Fusion gain metric $\beta\tau_E$ vs. plasma current in DIII-D. The colored points indicate the level of applied torque as given in the legend.*

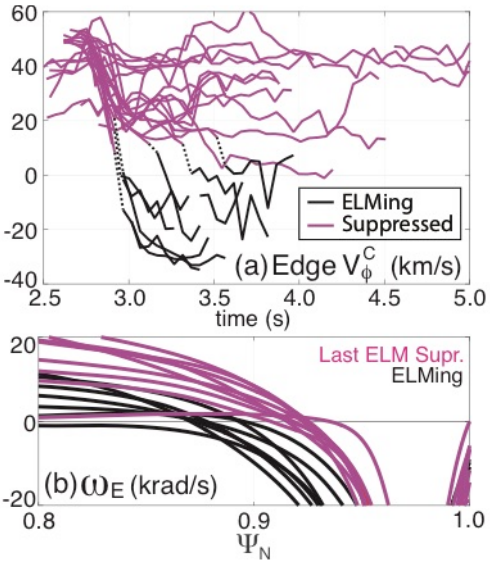


*FIG. 17. Low-torque ISS with applied n=3 RMP showing ELMing and ELM-suppresses cases: (a) edge rotation of carbon impurity, and (b) **E×B** rotation profile vs. normalized poloidal flux.*

A key result from IBS experiments in DIII-D is that stable (although dense) plasmas with zero injected torque can achieve normalized plasma pressures capable of generating 500 MW of fusion power in ITER, as well as a fusion gain metric insensitive to plasma current between 2.8≤ $q_{95}$≤3.7 [34]. For this study, a DIII-D shape well matched to the ITER separatrix is used such that a normalized current ($I_P/aB_T$) of 1.4 yields $q_{95}$≈3. Plasma current scans are performed with three levels of injected beam torque: full co-NBI, 1 Nm and zero torque. Feedback control of the neutral beams maintains simultaneously the normalized pressure and injected torque using duty cycle modulation of the co- and counter-sources. For co-NBI a volume average beta of 2.55%, able to produce 500 MW of fusion power in ITER, is reached for $q_{95}$≈4.2, while for zero injected torque β=2.55% is reached around $q_{95}$≈3.4. Stable operation with zero injected torque is obtained down to $q_{95}$=2.8; it has been shown for IBS cases in DIII-D that MHD stability at zero torque is due to changes in the current density profile and not the rotation profile directly [35]. The fusion gain metric ($\beta\tau_E$) shows saturation with decreasing $q_{95}$ for all levels of applied torque (see Fig. 16). The same $\beta\tau_E$ is obtained for $q_{95}$=3.7 as for $q_{95}$=2.8 with zero injected torque, but the lower current case has lower disruption risk. Further work in IBS development in DIII-D is needed to extend the zero injected torque plasmas to lower density to better match ITER's $\nu_*$.

Previous work has demonstrated that ELM suppression with $n$=3 RMP in the IBS is lost when the injected NBI torque is reduced below ~4 Nm [36]. Experiments on DIII-D have since focused on resolving the cause of this apparent rotation threshold by conducting NBI torque scans using co- and counter-$I_P$ sources in the ISS with $q_{95}$=3.5 [37]. Figure 17(a) shows that a clear and consistent edge carbon impurity rotation threshold ($V_*$) for maintaining RMP ELM suppression of about 10 km/s is found (Mach no. $M_*$~0.1) regardless of core plasma pressure. Within the field penetration paradigm for ELM suppression [38], this can be explained by an inward motion of the zero-crossing of the flow, which moves the region of field penetration too far away from the pedestal top if rotation is too low [39]. Indeed, computing the ***E×B*** rotation profile ($\omega_E$) for the final ELM suppressed time-slice reveals a critical location for the $\omega_E$ zero-

crossing of $\Psi_N$=0.91 (Fig. 17(b)). Narrowing the pedestal by reducing the upper triangularity is found to move the critical $\omega_E$ zero-crossing radius outward, suggesting a critical distance between the pedestal top and the $\omega_E$ zero-crossing. These studies also are unable to find any critical condition for the electron perpendicular rotation, challenging two-fluid models of field penetration.

While no simple beam torque threshold describes the ELMing/suppressed boundary in Fig. 17, a negative value for the edge beam torque *density* is a good predictor of losing RMP ELM-suppression [37]. It is important to note that balanced NBI with "zero injected torque" is modeled by NUBEAM to yield a edge localized torque in the counter-$I_P$ direction owing to the loss of trapped counter beam ions after the first bounce (i.e., counter beam orbit loss torque). Therefore, rather than discuss ITER-relevant torques, a semi-quantitative requirement on ITER's edge rotation for RMP ELM-suppression is derived from the scaling of the toroidal flow required to sustain an $\omega_E$ zero-crossing. Along a dimensionally similar path, the Mach no. at $E_r$=0 scales like $M_\phi \sim q\rho_*$ (i.e., diamagnetic scaling) [13]. Thus, the $M_\phi$~0.1 threshold for the ISS on DIII-D scales to $M_\phi$~0.02 on ITER, which is an edge rotation of ~3 km/s or ~0.4 krad/s. This threshold estimate is well below the predicted edge rotation from intrinsic torque on ITER shown in Fig. 4(a) (albeit without RMP), indicating a favorable scaling for obtaining ELM-suppression in ITER.

Experiments in DIII-D have advanced the quiescent H-mode (QH-mode) regime toward becoming a natural solution to avoiding ELMs in a zero injected torque, high confinement scenario that is compatible with strong electron heating and ITER's collisionality. Investigations of the newly developed wide-pedestal QH-mode, which exhibits a transport-limited pedestal regulated by broadband turbulence when the NBI torque is ramped from strongly counter-$I_P$ towards zero [40,41], have revealed that this regime can operate over a large range of NBI torques fully covering the scaled ITER-equivalent NBI torque. Most significantly, the strong counter-$I_P$ startup torque has been eliminated so that the entire discharge uses essentially zero (-0.04 to -0.06 Nm) NBI torque (see Fig. 18) [42]. The ~0 injected torque operation greatly benefits from using NTV from n=3 RMP fields to maintain enough plasma rotation to prevent core tearing modes from growing and locking. Turning off the NTV torque after formation of the wide-pedestal QH-mode has little effect. Also the operating space for wide-pedestal QH-mode has been expanded to include a lower-single-null configuration with the ITER triangularity value and a range of safety factors ($3.8<q_{95}<7.5$). Additionally, the wide-pedestal QH-mode regime has been sustained for several confinement times with dominant electron heating (3 MW ECH and 0.9 MW NB) and low (counter) torque. Depositing the ECH power at ρ=0.2 results in an electron internal transport barrier (ITB) with $T_e$ exceeding 12 keV. More generally, the observed improvement in both core and pedestal confinement as $T_e/T_i$ approaches 1 and the continued ELM-stable operation with high power ECH suggests that fast ions from NBI (including the associated counter beam orbit loss torque) are not a requirement for wide-pedestal QH-mode. Thus, QH-mode looks to be a promising ELM-stable scenario for ITER if fusion performance targets (β=2.55%, $q_{95}$≈3) can be reached — a key remaining challenge.

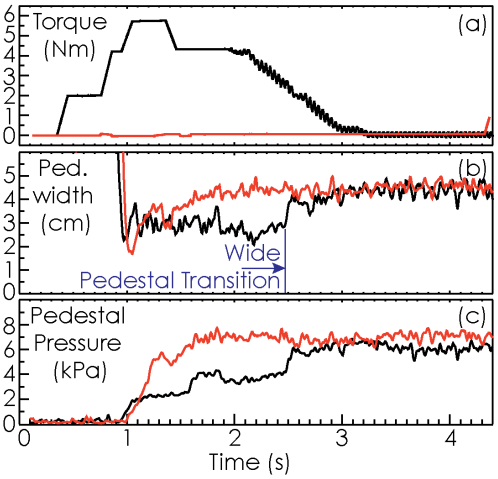


*FIG. 18. Wide pedestal QH-mode regime can be initiated and sustained with (black) and without (red) strong counter-$I_P$ startup torque from NBI.*

The high-$\beta_P$ scenario with high $q_{min}$ (≥3) has been extended inductively from $q_{95}$~11 to $q_{95}$~6 while maintaining an ITB and $H_{98y2}$ above 1.5 [43]. One of the key characteristics of this scenario is the large radius ITB in all transport channels, which is due to the Shafranov shift stabilization of turbulence at large $\beta_P$ [44]. These experiments utilize a second $I_P$ ramp up during the high beta phase ($\beta_N$~2.6–3.0) to increase the plasma current from 0.6 MA to 1.0 MA. The ITB can be maintained even as $\beta_P$ is reduced due to a strong reverse magnetic shear near ρ~0.5, confirming predictions that negative central shear can lower the $\beta_P$ threshold for the ITB, although ***E×B*** shear inside this radius may also play a role. Experiments at $q_{95}$ relevant for steady-state reactors have found two observed confinement states in the high-$\beta_P$ scenario, as exhibited in Fig. 19(a): (i) a H-mode confinement state with a high edge pedestal (dash lines), and (ii) an enhanced confinement state with a low pedestal and an ITB (solid lines). This can be explained through Shafranov shift stabilization creating a bifurcation in transport. The transition between these two confinement states may be related to changes in the pedestal region. When applying a large n=3 RMP to the high-$\beta_P$ scenario to mitigate large type-I ELMs, no transition is found to the enhanced confinement state which is otherwise observed with smaller n=3

perturbations. This is consistent with the hypothesis that a large edge perturbation may be needed to trigger the bifurcation to an ITB state. Pedestal stability analysis using ELITE shows that the high pedestal, H-mode state is limited by the current gradient, whereas the ITB state with low pedestal is far away from both the peeling and ballooning limits. Self-consistent modeling of this high-$\beta_P$ regime using the TGYRO code to predict the density and temperature profiles shows that the reverse magnetic shear and ITB can be maintained on ITER (Fig. 19(b)), leading to a $Q$=5 steady-state scenario.

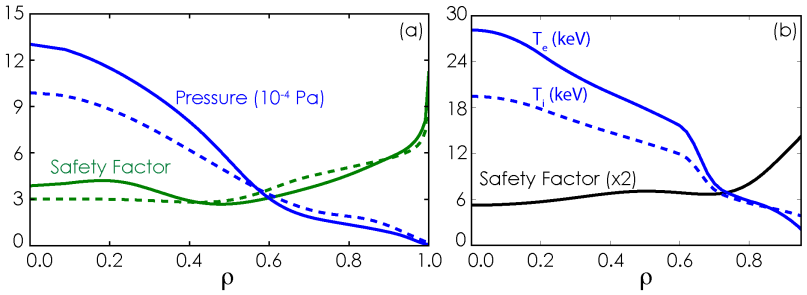


*FIG. 19. High $\beta_P$ scenario with $q_{95}$=6.5: (a) measured safety factor and pressure profiles for confinement states with and without reverse magnetic shear, and (b) TGYRO predictions for ITER steady-state scenario with reverse magnetic shear.*

Finally, a substantial expansion of the high-$\beta_N$ hybrid scenario to high density and radiating divertor operation has been achieved, and shows how the electron heating location impacts the effectiveness of a radiating mantle solution. Coupling a high-performance core to a divertor with acceptable heat flux is a crucial step for any fusion reactor. Previously DIII-D developed a low-collisionality steady-state hybrid scenario with $q_{95}$=5.5–6.5 that reaches ~85% of the ideal MHD "with wall" $\beta_N$ limit and scales to $Q$=5 on ITER [45,46]. To integrate this scenario with divertor heat flux mitigation using the "puff-and-pump" technique entails increasing the pedestal density by ~50% or more, which requires moving ECH from ρ~0.05-0.2 to ρ=0.45 to avoid the density cutoff [47]. These experiments find that higher density improves confinement and pedestal height at high heating power ($P_{tot}$>12 MW), partially due to improved pedestal stability from decoupling of the peeling and ballooning branches [48]. While these plasmas run reliably with $\beta_N \leq 3.8$, $H_{98y2}$=1.6 and 56 MJ of injected energy from ECH and NBI, the change in ECH location has a strong effect on the profiles of the neon and argon ions used to create a radiating mantle. For off-axis ECH, the density profile peaking factor is ~2.6 for neon and ~3.2 for argon, both of which are more peaked than the electron density profile (~1.4); for on-axis ECH, the neon profile is flat and no accumulation is observed (Fig. 20). Radiating emissivity measurements show an increased radiative peaking in the edge region (as desired for a radiating mantle) compared to cases without impurities; however, an increase in core radiation due to central impurity accumulation with off-axis ECH is correlated with significant fuel dilution and an onset of 5/2 and/or 3/1 tearing modes. Owing to the impurity/MHD complications with off-axis ECH, so far a modest 40% reduction in between-ELM divertor heat flux has been achieved with argon-based and neon-based mantles, as displayed in Fig. 21 [49]. A low injected torque is also a necessary condition for reactor-relevant studies, and this has been assessed in the high-$\beta_N$ hybrid regime using a mixture of co- and counter-NBI. Scanning the NBI torque from 8.5 Nm (full co-injection) to 0.5 Nm (best match of co- and counter-NBI power), up to the available 4.5 MW of counter-NBI power, finds that the $H_{98y2}$ factor systematically decreases from 1.55 to 1.07. For the lowest torque condition, the $H_{98y2}$ factor is independent of ECH power. Future experiments will combine low injected torque and radiative divertor operation by utilizing increased ECH power with a higher density limit (either from higher frequency gyrotrons or 2nd harmonic O-mode absorption) and central deposition, along with improved divertor closure to help localize impurity pumping, to prevent central impurity accumulation.

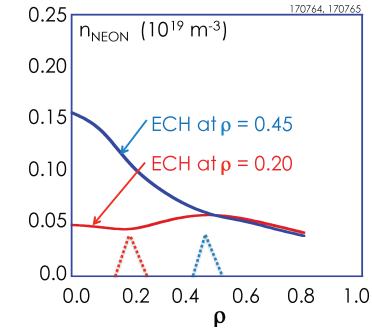


*FIG. 20. Neon density profiles for two ECH locations in high-$\beta_N$ hybrid scenario with radiative divertor.*

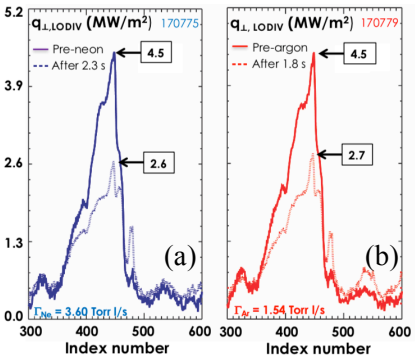


*FIG. 21. Measured divertor heat flux reduction for radiating mantle in high-$\beta_N$ hybrid scenario: (a) neon, and (b) argon.*

## 5. SUMMARY AND FUTURE PLANS

The DIII-D program is addressing critical challenges for ITER and the next generation of fusion devices through research on plasma physics fundamentals, integration of disparate core and boundary plasma physics, and development of attractive scenarios. Disruption mitigation experiments injecting multiple shattered pellets find

that simultaneously injected pellets may impact the assimilation of each other and alter the resulting disruption characteristics. Better resolved measurements and more comprehensive modeling of RE dissipation on DIII-D have provided a resolution to widely observed anomalous RE dissipation results [50], improving confidence that RE mitigation and avoidance can be predictively optimized. The inclusion of a *kick model* for EP transport in TRANSP has resulted in a dramatic improvement in simulating fast-ion transport during strong Alfvénic activity and tearing modes. Measurements of the $\rho_*$ dependence of intrinsic rotation in ECH H-modes find similar $\rho_*$ scaling as for NBI H-modes, and the predicted $\boldsymbol{E\times B}$ rotational shear for ITER is large enough to give significant turbulence stabilization. In boundary physics, UEDGE multi-fluid simulations show that the $\boldsymbol{E\times B}$-drifts can explain the sharp onset of detachment since a positive feedback mechanism helps the density to rise more rapidly and accelerate detachment. Detached divertor plasmas display characteristics of convection dominated transport with parallel plasma flows towards the divertor target of M~1. Recent model validation studies conclude that energetic free-streaming $D^+$ ions and $C^{6+}$ impurities from the pedestal top typically dominate the intra-ELM gross erosion of W in the DIII-D divertor.

In core-edge integration, experiments with the new SAS divertor achieved a significant reduction in $T_e$ across the divertor target and access to dissipative divertor operation at lower density with respect to the other two (open/closed) divertor configurations on DIII-D. At high SOL opacity, gas puffing does not appear to play a direct role in raising the pedestal density since the particle source inside the separatrix is actually reduced; the ionized plasma in the SOL may flow to the outer detached divertor leg and recycle. A more closed divertor configuration is found to reduce core ionization and flatten the density pedestal, although a large gradient of pedestal $T_e$ can be maintained. Using a rotating $n$=2 RMP combined with a stationary $n$=3 RMP, the equivalent coil current for ELM suppression is reduced by ~30% and the fine structure in the divertor heat and particle fluxes are smoothed out. The increase in $P_{LH}$ with RMP is higher for ITER relevant collisionalities and is likely explained by a reduction in the edge $E_r$ well and $\boldsymbol{E\times B}$ shear from edge magnetic stochasticity. In the Super H-mode regime, very high pedestal pressure (>20 kPa) and core confinement are sustained with a strongly radiating divertor and a >2× reduction in divertor electron temperature.

A key advance in scenario development has been the achievement of stable (although dense) ITER baseline discharges with zero injected torque and a fusion gain metric insensitive to plasma current between $2.8\leq q_{95}\leq 3.7$. For RMP ELM suppression in the ITER similar shape ($q_{95}$=3.5), a clear and consistent threshold in the impurity rotation of ~10 km/s is observed at which point ELM suppression is lost, possibly due to the inward motion of the $\omega_E$ zero-crossing; fortunately, this scales to a threshold value in ITER that is less than the expected pedestal rotation from intrinsic torque. In the wide pedestal QH-mode regime that exhibits improved performance, the counter-$I_P$ startup torque has been eliminated so that the entire discharge uses ≈0 injected NBI torque, and a low-torque regime has been sustained with dominant electron heating. The high-$\beta_P$ scenario with high $q_{min}$ (≥3) has been extended inductively from $q_{95}$~11 to $q_{95}$~6 while maintaining an ITB with the help of strong reverse magnetic shear near ρ~0.5. The high-$\beta_N$ hybrid scenario has been extended to high density and radiating divertor operation with $\beta_N\leq 3.8$ and $H_{98y2}$=1.6; both argon-based and neon-based radiating mantles achieve a 40% reduction in divertor heat flux but a large difference in core impurity peaking is observed between central and off-axis ECH deposition. These scenario experiments have made substantial progress in integrating all of the necessary ingredients for a burning plasma device: low torque, ELM suppression, electron heating, confinement and pedestal enhancement, high density, radiating divertors and impurity transport.

After 2018, DIII-D research will orient further to the steady-state path [51], doubling its off-axis NBI power by vertically tilting two beam sources as well as making them toroidally steerable for co- or counter-injection, and doubling the electron cyclotron power to raise $T_e/T_i$ at low torque, increase off-axis current drive and allow perturbative transport studies under high performance conditions. DIII-D will also explore new methods of high efficiency off-axis current drive to optimize the high-beta, steady-state path, including top-launch ECCD and 1 MW helicon wave current drive at 476 MHz in 2019, and inside-launch LHCD soon after. We are currently optimizing the alignment of the upper SAS tiles with the toroidal field and associated diagnostic upgrades. This is accompanied by plans for new high-Z tiles in the upper SAS divertor to enable study of high-Z leakage from closed divertors, and in the future more reactor-relevant pumped slot divertors. Disruption mitigation research will test silicon shell pellets filled with silicon or boron. Additional power supplies and a new 3D coil set are planned to explore the physics basis for optimization of ELM and MHD control. Critical physics questions will be addressed with new diagnostics including multi-channel divertor Thomson scattering to inform detachment studies, divertor charge exchange spectroscopy for $T_i$ measurements, expanded 3D-magnetic diagnostics, EUV imaging to look at the earliest stages of runaway electron formation, a fast ion loss detector optimized for reverse $B_T$ direction (preferred for off-axis NBI), a wall interaction tile station for rapid evaluation of first wall materials and PMI, imaging MSE, and expansions and upgrades to the existing suite of turbulence diagnostics.

## ACKNOWLEDGEMENTS

This material is based upon work supported by the U.S. Department of Energy, Office of Science, Office of Fusion Energy Sciences, using the DIII-D National Fusion Facility, a DOE Office of Science user facility, under Awards DE-FC02-04ER54698. DIII-D data shown in this paper can be obtained in digital format by following the links at https://fusion.gat.com/global/D3D_DMP. **Disclaimer:** This report was prepared as an account of work sponsored by an agency of the United States Government. Neither the United States Government nor any agency thereof, nor any of their employees, makes any warranty, express or implied, or assumes any legal liability or responsibility for the accuracy, completeness, or usefulness of any information, apparatus, product, or process disclosed, or represents that its use would not infringe privately owned rights. Reference herein to any specific commercial product, process, or service by trade name, trademark, manufacturer, or otherwise does not necessarily constitute or imply its endorsement, recommendation, or favoring by the United States Government or any agency thereof. The views and opinions of authors expressed herein do not necessarily state or reflect those of the United States Government or any agency thereof.

## REFERENCES

[1] AYMAR, R., Plasma Phys. Control. Fusion **44** (2002) 519.
[2] HERFINDAL, J.L., et al., this conference, EX/P6-23.
[3] PAZ-SOLDAN, C., et al., Phys. Rev. Lett. **118** (2017) 255002.
[4] PAZ-SOLDAN, C., et al., this conference, EX/6-1.
[5] LIU, C., et al., Phys. Rev. Lett. **120** (2018) 265001.
[6] SPONG, D.A., et al., Phys. Rev. Lett. **120** (2018) 155002.
[7] THOME, K.E., et al., this conference, EX/P6-29.
[8] SPONG, D.A., et al., this conference, TH/P8-17.
[9] PODESTA, M., et al., Plasma Phys. Control. Fusion **59** (2017) 095008.
[10] PODESTA, M., et al., this conference, EX/1-2.
[11] CHRYSTAL, C., et al., Phys. Plasmas **24** (2017) 056113.
[12] DEGRASSIE, J.S., et al., Phys. Plasmas **23** (2016) 082501.
[13] CHRYSTAL, C., et al., this conference, EX/5-2.
[14] HOWARD, N.T., et al., to be submitted to Rev. Sci. Instrum. (2018).
[15] STAEBLER, G.M., KINSEY, J.E., Phys. Plasmas **17** (2010) 122309.
[16] BELLI, E.A., CANDY, J., Plasma Phys. Control. Fusion **50** (2008) 095010.
[17] AUSTIN, M.E., et al., this conference, EX/6-6.
[18] JAERVINEN, A.E., et al., Phys. Rev. Lett. **121** (2018) 075001.
[19] JAERVINEN, A.E., et al., this conference, EX/9-3.
[20] LEONARD, A.W., et al., this conference, EX/P6-12.
[21] DING, R., et al., this conference, MPT/2-2.
[22] ABRAMS, T., et al., this conference, EX/P6-13.
[23] GUO, H.Y., et al., Nucl. Fusion **57** (2017) 044001.
[24] GUO, H.Y., et al., this conference, EX/P6-10.
[25] MORDIJCK, S., et al., this conference, EX/P6-5.
[26] WANG, H.Q., et al., Nucl. Fusion **58** (2018) 096014.
[27] HINSON, E.T., et al., this conference, EX/P6-18.
[28] SUN, Y., et al., this conference, EX/7-2.
[29] SCHMITZ, L., et al., this conference, EX/4-2.
[30] MORDIJCK, S, et al., Plasma Phys. Control. Fusion **58** (2016) 014003.
[31] SOLOMON, W., et al., Phys. Rev. Lett. **113** (2014) 135001.
[32] SNYDER, P.B., et al., Nucl. Fusion **55** (2015) 083026.
[33] SNYDER, P.B., et al., this conference, EX/2-4.
[34] LUCE, T.C., et al., this conference, PPC/2-1.
[35] TURCO, F., et al., Nucl. Fusion **58** (2018) 106053.
[36] MOYER, R.A., et al., Phys. Plasmas **24** (2017) 102501.
[37] PAZ-SOLDAN, C., et al., to be submitted to Nucl. Fusion (2018).
[38] NAZIKIAN, R., et al., Phys. Rev. Lett. **114** (2015) 105002.
[39] LYONS, B.C., et al., Plasma Phys. Control. Fusion **59** (2017) 044001.
[40] BURRELL, K.H., et al., Phys. Plasmas **23** (2016) 056103.
[41] CHEN, XI, et al., Nucl. Fusion **57** (2017) 022007.
[42] ERNST, D.R., et al., this conference, EX/2-2.
[43] MCCLENANGHAN, J., et al., this conference, EX/4-3.
[44] GAROFALO, A.M., et al., Phys. Plasmas **24** (2017) 056114.
[45] TURCO, F., et al., Phys. Plasmas **22** (2015) 056113.
[46] PETTY, C.C., et al., Nucl. Fusion **56** (2016) 016016.
[47] TURCO, F., et al., this conference, EX/3-3.
[48] PETRIE, T.W., et al., Nucl. Fusion **57** (2017) 086004.
[49] PETRIE, T.W., et al., this conference, EX/P6-11.
[50] GRANETZ, R., et al., Phys. Plasmas **21** (2014) 072506.
[51] BUTTERY, R.J., et al., J. Fusion Energ. (2018) https://doi.org/10.1007/s10894-018-0185-y.

# APPENDIX: THE DIII-D TEAM

L. Abadie[1], T.W. Abrams[2], J. Ahn[3], T. Akiyama[4], P. Aleynikov[5], J. Allcock[6], E.O. Allen[2], S. Allen[7], J.P. Anderson[2], A. Ashourvan[8], M.E. Austin[9], J. Bak[10], K.K. Barada[11], N. Barbour[8], L. Bardoczi[12], J. Barr[2], J.L. Barton[13], E.M. Bass[14], D. Battaglia[8], L.R. Baylor[3], J. Beckers[15], E.A. Belli[2], J.W. Berkery[16], N. Bertelli[8], J.M. Bialek[16], J.A. Boedo[14], R.L. Boivin[2], P.T. Bonoli[17], A. Bortolon[8], M.D. Boyer[8], R.E. Brambila[2], B. Bray[2], D.P. Brennan[8], A.R. Briesemeister[3], S.A. Bringuier[2], M.W. Brookman[2], D.L. Brower[11], B.R. Brown[2], W.D. Brown[8], D. Buchenauer[13], M.G. Burke[18], K.H. Burrell[2], J. Butt[8], R.J. Buttery[2], I. Bykov[14], J.M. Candy[2], J.M. Canik[3], N.M. Cao[17], L. Carbajal Gomez[3], L.C. Carlson[2], T.N. Carlstrom[2], T.A. Carter[11], W. Cary[2], L. Casali[12], M. Cengher[2], V.S. Chan[19], B. Chen[19], J. Chen[20], J. Chen[11], M. Chen[21], R. Chen[20], Xi Chen[2], W. Choi[16], C. Chrobak[2], C. Chrystal[2], R.M. Churchill[8], M. Cianciosa[3], C.F. Clauser[14], M. Clement[16], J. Coburn[22], C.S. Collins[2], A.W. Cooper[23], B.M. Covele[2], J.W. Crippen[2], N.A. Crocker[11], B.J. Crowley[2], A. Dal Molin[24], E.M. Davis[17], J.S. deGrassie[2], C.A. del-Castillo-Negrete[25], L.F. Delgado-Aparicio[8], A. Diallo[8], S.J. Diem[3], R. Ding[12], S. Ding[12], W. Ding[11], J.L. Doane[2], D.C. Donovan[26], J. Drake[2], D. Du[2], H. Du[27], X. Du[28], V. Duarte[8], J.D. Duran[26], N.W. Eidietis[2], D. Elder[29], D. Eldon[2], W. Elwasif[3], T.E. Ely[2], K.M. Eng[2], K. Engelhorn[2], D. Ennis[30], K. Erickson[8], D.R. Ernst[17], T.E. Evans[2], M.E. Fenstermacher[7], N.M. Ferraro[8], J.R. Ferron[2], D.F. Finkenthal[31], P.A. Fisher[8], B. Fishler[2], S.M. Flanagan[2], J.A. Fooks[2], L. Frassinetti[32], H.G. Frerichs[18], Y. Fu[33], T. Fulop[34], Q. Gao[27], F. Garcia[2], A.M. Garofalo[2], A. Gattuso[2], L. Giacomelli[35], E.M. Giraldez[2], C. Giroud[36], F. Glass[2], P. Gohil[2], X. Gong[20], Y.A. Gorelov[2], R.S. Granetz[17], D.L. Green[37], C.M. Greenfield[2], B.A. Grierson[8], R.J. Groebner[2], W.H. Grosnickle[2], M. Groth[38], H.J. Grunloh[2], H.Y. Guo[2], W. Guo[20], J. Guterl[12], R.C. Hager[8], S. Hahn[10], F.D. Halpern[2], H. Han[39], M.J. Hansink[2], J.M. Hanson[16], J. Harris[2], S.R. Haskey[8], D.R. Hatch[9], W.W. Heidbrink[28], J. Herfindal[3], D.N. Hill[2], M.D. Hill[40], E.T. Hinson[18], C.T. Holcomb[7], C.G. Holland[14], L.D. Holland[2], E.M. Hollmann[14], A.M. Holm[38], R. Hong[12], M. Hoppe[34], S. Houshmandyar[9], J. Howard[41], N.T. Howard[17], Q. Hu[8], W. Hu[20], H. Huang[2], J. Huang[20], Y. Huang[20], G.A. Hughes[2], J. Hughes[17], D.A. Humphreys[2], A.W. Hyatt[2], K. Ida[4], V. Igochine[5], Y. In[42], S. Inoue[43], A. Isayama[43], R.C. Isler[3], V.A. Izzo[14], M.R. Jackson[2], A.E. Jarvinen[7], Y. Jeon[10], H. Ji[33], X. Jian[19], R. Jimenez[2], C.A. Johnson[30], I. Joseph[7], D.N. Kaczala[2], D.H. Kaplan[2], J. Kates-Harbeck[44], A.G. Kellman[2], D.H. Kellman[2], C.E. Kessel[8], K. Khumthong[2], C.C. Kim[45], H. Kim[10], J. Kim[46], K. Kim[12], S.H. Kim[1], W. Kimura[47], J.R. King[48], A. Kirk[36], K. Kleijwegt[15], M. Knolker[8], A. Kohn[5], E. Kolemen[8], M. Kostuk[2], G.J. Kramer[8], P. Kress[49], D.M. Kriete[18], R.J. La Haye[2], F.M. Laggner[33], H. Lan[20], M.J. Lanctot[2], R. Lantsov[11], L.L. Lao[2], C.J. Lasnier[7], C. Lau[12], K. Law[3], D. Lawrence[50], J. Le[51], R.L. Lee[2], M. Lehnen[1], R. Leon[2], A.W. Leonard[2], M. Lesher[2], J.A. Leuer[52], G. Li[20], K. Li[20], K.T. Liao[9], Z. Lin[28], C. Liu[2], C. Liu[8], F. Liu[53], Y. Liu[2], Z. Liu[20], S. Loch[30], N.C. Logan[8], J.M. Lohr[2], J. Lore[3], T.C. Luce[1], N.C. Luhmann[21], R. Lunsford[8], C. Luo[21], Z. Luo[20], L. Lupin-Jimenez[8], A. Lvovskiy[12], B.C. Lyons[2], X. Ma[12], R. Maingi[8], M.A. Makowski[7], P. Mantica[54], M. Manuel[2], M.W. Margo[2], A. Marinoni[17], E. Marmar[17], W.C. Martin[2], R.L. Masline[14], G.K. Matsunaga[43], D.M. Mauzey[8], P.S. Mauzey[2], J.T. Mcclenaghan[12], G.R. Mckee[18], A.G. Mclean[7], H.S. Mclean[7], E. Meier[55], S.J. Meitner[3], J.E. Menard[8], O. Meneghini[2], G. Merlo[11], W.H. Meyer[7], D.C. Miller[2], W.J. Miller[2], C.P. Moeller[2], K.J. Montes[17], M.A. Morales[2], S. Mordijck[49], A. Moser[2], R.A. Moyer[14], S.A. Muller[2], S. Munaretto[2], M. Murakami[3], C.J. Murphy[2], C.M. Muscatello[2], C.E. Myers[13], A. Nagy[8], G.A. Navratil[16], R.M. Nazikian[8], A.L. Neff[37], T.F. Neiser[11], A. Nelson[33], P. Nguyen[2], R. Nguyen[2], J.H. Nichols[26], M. Nocente[24], R.E. Nygren[13], R.C. O'Neill[2], T. Odstrcil[17], S. Ohdachi[4], M. Okabayashi[8], E. Olofsson[2], M. Ono[43], D.M. Orlov[14], T.H. Osborne[2], N.A. Pablant[8], D.C. Pace[2], R.R. Paguio[2], A. Pajares Martinez[56], C. Pan[20], A. Pankin[48], J.M. Park[3], J. Park[8], Y. Park[16], C.T. Parker[2], S.E. Parker[57], P.B. Parks[2], C.J. Pawley[2], C.A. Paz-Soldan[2], W.A. Peebles[11], B.G. Penaflor[2], T.W. Petrie[2], C.C. Petty[2], Y. Peysson[58], A.Y. Pigarov[14], D.A. Piglowski[2], R.I. Pinsker[2], P. Piovesan[59], N. Piper[40], R.A. Pitts[1], J.D. Pizzo[60], M.L. Podesta[8], F.M. Poli[8], D. Ponce[2], M. Porkolab[17], G.D. Porter[61], R. Prater[2], J. Qian[20], O. Ra[42], T. Rafiq[56], R. Raman[55], C. Rand[2], G.C. Randall[2], J.M. Rauch[2], C. Rea[17], M.L. Reinke[3], J. Ren[26], Q. Ren[20], Y. Ren[8], T.L. Rhodes[11], J. Rice[17], T.D. Rognlien[7], J.C. Rost[17], W.L. Rowan[9], D.L. Rudakov[14], A. Salmi[62], B.S. Sammuli[2], C.M. Samuell[7], A.M. Sandorfi[63], C. Sang[64], O.J. Sauter[65], D.P. Schissel[2], L. Schmitz[11], O. Schmitz[18], E.J. Schuster[56], J.T. Scoville[2], A. Seltzman[17], I. Sfiligoi[2], M. Shafer[3], H. Shen[2], T. Shi[20], D. Shiraki[3], H. Si[20], D.R. Smith[18], S.P. Smith[2], J.A. Snipes[1], P.B. Snyder[2], E.R. Solano[66], W.M. Solomon[2], A.C. Sontag[3], V.A. Soukhanovskii[7], D.A. Spong[3], W.M. Stacey[40], G.M. Staebler[2], L. Stagner[12], B. Stahl[2], P.C. Stangeby[29], T.J. Stoltzfus-Dueck[8], D.P. Stotler[8], E.J. Strait[2], D. Su[2], L.E. Sugiyama[17], A.A. Sulyman[21], Y. Sun[20], C. Sung[67], W.A. Suttrop[5], Y. Suzuki[4], A. Svyatkovskiy[33], R.M. Sweeney[1], S. Taimourzadeh[28], M. Takechi[43], T. Tala[62], H. Tan[20], S. Tang[11], X. Tang[68], D. Taussig[2], G. Taylor[8], N.Z. Taylor[12], T.S. Taylor[2], A. Teklu[69], D.M. Thomas[2], M.B. Thomas[70], K.E. Thome[12], A.R. Thorman[41], R.A. Tinguely[17], B.J. Tobias[68], J.F. Tooker[2], H. Torreblanca[2], A. Torrezan De Sousa[2], G.L. Trevisan[12], D. Truong[18], F. Turco[16], A.D. Turnbull[2], E.A. Unterberg[3], P. Vaezi[14], P.J. Vail[33], M.A. Van Zeeland[2], M. Velasco Enriquez[71], M.C. Venkatesh[2], B.S. Victor[7], F. Volpe[16], M.R. Wade[2], M.L. Walker[2], J.R. Wall[2], G.M. Wallace[17], R.E. Waltz[2], G. Wang[11], H. Wang[20], H. Wang[12], Y. Wang[21], Y. Wang[20], Z. Wang[68], Z. Wang[8], F. Wang[64], S.H. Ward[70], J.G. Watkins[13], M. Watkins[2], W.P. Wehner[56], M. Weiland[5], D.B. Weisberg[2], A.S. Welander[2], A.E. White[17], R.B. White[8], D. Whyte[17], T.A. Wijkamp[15], R. Wilcox[3], T. Wilks[17], H.R. Wilson[70], A. Wingen[3], E. Wolfe[8], M. Wu[20], W. Wu[2], S.J. Wukitch[17], T. Xia[20], N. Xiang[20], B. Xiao[20], R. Xie[9], G. Xu[19], H. Xu[2], X. Xu[7], Z. Yan[18], Q. Yang[20], X. Yang[64], M. Yoshida[43], G. Yu[21], J.H. Yu[14], M. Yu[10], S.A. Zamperini[26], L. Zeng[11], B. Zhao[9], D. Zhao[12], H. Zhao[9], Y. Zhao[72], Y. Zhu[21], Y. Zhu[28], B. Zywicki[73]

# AFFILIATIONS


[1]ITER Organization
[2]General Atomics
[3]Oak Ridge National Laboratory
[4]National Institute for Fusion Science, Japan
[5]Max-Planck Institute for Plasma Physics
[6]Durham University
[7]Lawrence Livermore National Laboratory
[8]Princeton Plasma Physics Laboratory
[9]University of Texas, Austin
[10]National Fusion Research Institute, Korea
[11]University of California, Los Angeles
[12]Oak Ridge Associated Universities
[13]Sandia National Laboratory
[14]University of California, San Diego
[15]Eindhoven Unversity of Technology
[16]Columbia University
[17]Massachusetts Institute of Technology
[18]University of Wisconsin
[19]University of Science and Technology of China
[20]Institute of Plasma Physics, Chinese Academy of Sciences
[21]University of California, Davis
[22]North Carolina State
[23]EPFL (Lausanne, Switzerland)
[24]Universita di Milano-Bicocca
[25]Stony Brook University (SUNY)
[26]University of Tennessee, Knoxville
[27]Southwestern Institute of Physics, China
[28]University of California, Irvine
[29]University of Toronto
[30]Auburn University
[31]Palomar College
[32]Kungliga Tekniska Hogskolan
[33]Princeton University
[34]Chambers University of Technology (Sweden)
[35]Istituto di Fisica del Plasma CNR-EURATOM
[36]United Kingdom Atomic Energy Authority (CCFE)
[37]Oak Ridge Institute for Science Education
[38]Aalto University
[39]Korea National Fusion Research Center
[40]Georgia Tech
[41]Australian National University
[42]Ulsan National Institute of Science and Technology
[43]National Institutes for Quantum and Radiological Science, Japan
[44]Harvard University
[45]SLS2 Consulting
[46]Far-Tech, Inc.
[47]STI Optronics, Inc.
[48]Tech-X Corporation
[49]The College of William and Mary
[50]General Atomics Temp
[51]Qinzhou University
[52]General Atomics (Retired)
[53]University of Nice
[54]IFP - Consiglio Nazionale delle Ricerche
[55]University of Washington
[56]Lehigh University
[57]University of Colorado, Boulder
[58]CEA Cadarache
[59]Consorzio RFX
[60]Rensselaer Polytechnic Institute
[61]AKIMA Infrastructure Services, LLC
[62]VTT Technical Research Centre
[63]Jefferson Lab
[64]Dalian University of Technology, China
[65]SPC-EPFL
[66]Ciemat
[67]Lam Research Corporation
[68]Los Alamos National Laboratory
[69]Oregon State University
[70]University of York
[71]Universidad Nacional de Ingenieria
[72]Soochow University
[73]University of Michigan